

Geochemistry and Tectonic Setting of the Eshan Granites in the Southwestern Margin of the Yangtze Plate, Yunnan

Jin Huⁱⁿ, Shitao Zhang^{in*}, Guangzheng Zhang, Siyu Tao, Ying Zhang

Faculty of Land Resource Engineering, Kunming University of Science and Technology, Kunming 650093, China

ⁱⁿJin Hu: <https://orcid.org/0000-0003-3805-7611>; ⁱⁿShitao Zhang: <https://orcid.org/0000-0002-8901-9255>

ABSTRACT: The extensive Eshan granites of Yunnan are made up of three intrusive units distinguished by their field contact relations; in descending order of age they are the Pojiao Unit, the Lüzicun Unit and the Mokela Unit. The Pojiao Unit and Lüzicun Unit contain petrographically and geochemically similar rocks but contact relationships show that the latter is younger. The Mokela Unit mainly consists of dykes intruding the other two and has petrographic and geochemical differences. Zircon U/Pb dating and zircon crystallization temperature measurements confirm the sequence of intrusions. Major and trace element analyses suggest that the magmas of the Pojiao Unit granites derived by partial melting of a clay-poor source from the upper crust; the magmas of the Lüzicun Unit granites derived by partial melting of upper crust with a small proportion of middle crust accompanied by crystallization of albite which triggered strength reduction. Both magmas mixed and underwent with crustal contamination, assimilation and fractional crystallization. The magmas of the Mokela Unit derived from residual melts and assimilation of argillaceous rocks. A time sequence of melting, intrusion and deformation events is derived from these results and compared with other published tectonic models for the evolution of the SW margin of the Yangtze Plate. Magmatism was initiated by exhumation of upper continental crust during which strongly peraluminous porphyritic biotite monzogranite granites were produced at ca. 854–852 Ma, and the genesis of two-mica granite reflected a later batch of exhumed melts with crustal contamination, assimilation and fractional crystallization at ca. 842 Ma. Finally biotite alkali-feldspar granite and tourmaline granite magmas experienced strong fractional crystallization, emplaced in the cooling stage at ca. 823 Ma, indicating the end of exhumation.

KEY WORDS: Yangtze Plate, Eshan, granite, tectonic evolution, continental exhumation, post-collision.

0 INTRODUCTION

The Eshan granite is located in the southwestern margin of the Yangtze Plate. Different views have been published about the nature of the substantial volume of acidic and minor basic magmatic rocks exposed in the western margin of the Yangtze Plate that were intruded at 850–740 Ma. Alternative theories consider their mode of formation in the context of a split of a Greenville orogenic belt within the Rodinia supercontinent, possible superplumes and related magmatism. There are three general views regarding the tectonic setting.

(1) The plate-island arc hypothesis considers that South China was a land mass surrounded by subduction zones in the Neoproterozoic era. Neoproterozoic magmatic rocks in different regions correspond to different types of arc magmatism (Du et al., 2013; Zhou J C et al., 2005; Zhou M F et al., 2002).

(2) The plume-rift hypothesis considers that between 830–740 Ma there was a superplume under the Rodinia supercontinent which caused the splitting of Rodinia supercontinent and widespread bimodal magmatism (Li X H et al., 2012, 2003; Li Z X et al., 2008).

(3) The plate-rift hypothesis regards plate subduction as an important mechanism for exchanging the mass and energy between the mantle and the crust, and igneous rocks in subduction zones as important carriers in the recycling of crustal materials and crust-mantle interaction (Song et al., 2015). This study presents evidence for recycling of crustal materials from the Sibao orogeny to Nanhua rifting in continental collision orogens of South China in the following stages; (a) detachment between continental crust and underlying lithospheric mantle; (b) decoupling between upper crust and lower crust; (c) detachment between superficial sedimentary cover and crystalline basement that have given rise to two types of magmatic rocks in arc-continent collisional orogenic belts. The early magmatic rocks are mainly products of extension caused by collapse of existing arc-continent collisional orogenic belts, which can include both juvenile crust and products of ancient crustal reconstruction. The late magmatic rocks are mainly products of continental rift activ-

*Corresponding author: taoge Zhang@hotmail.com

© China University of Geosciences and Springer-Verlag GmbH Germany, Part of Springer Nature 2018

Manuscript received July 11, 2016.

Manuscript accepted March 10, 2017.

ity that gave rise to both successful and failed rifts in different places (Zhao et al., 2013; Zheng et al., 2013a, b, c).

The Eshan granite is located at the southern tip of the Xikang-Yunnan axis in the southwestern margin of the Yangtze Plate. Zheng et al. (2007) and Li X H et al. (2003) have dated the Eshan pluton at 818 ± 10 Ma using SHRIMP U-Pb geochronology and thus dated the magmatic rocks as Late Neoproterozoic. There are at least three types of granite in that pluton. What are their emplacement relationships? Were they derived from synchronous, consanguineous magmas? We launched the present study of the Eshan granite to investigate its formation and tectonic evolution and resolve these questions.

1 GEOLOGICAL BACKGROUND

The Eshan granite is located in the Eshan-Shiping District of Yuxi City, Yunnan. It is one of the largest exposed granitoid bodies (approximately 200 km^2) in the southwestern margin of the Yangtze Craton, South China. The pluton was emplaced in a regime dominated by extension following the subduction of the Cathaysia Block beneath the Yangtze Block, a collisional amalgamation that occurred during the Sibao orogeny (Li X H et al., 2012, 2003; Li Z X et al., 2008; Wang, 2000). In the slab subduction and roll-backstage, voluminous granitic magmas were generated and emplaced around Sibao suture zone which is located from the Jiangshao fault in the NE, along the Geyang-Yichun-Pingxiang fault and Chaling-Changning-Daoxian fault, to Central Yunnan in the southwest (Wang et al., 1996). The Cathaysia and Yangtze blocks first came together at the southwestern margin of the Yangtze Plate (Li X H et al., 2012), and clastic sediments from the Cathaysia Block characterized by zircons of the 1 430 Ma Baoban granite were deposited in the foreland basin as the Kunyang Group and corresponding strata. The timing of elimination of oceanic crust between the continents can be estimated from the ages of the youngest ophiolites, arc volcanic rocks and HP metamorphic rocks. For instance in the Sibao orogen, the youngest greenschist facies metamorphic rocks formed at 940 Ma in Tianli at the southeast margin of the Yangtze Craton. The youngest arc volcanic rocks (Shuangxiwu) formed at 890 Ma, and the youngest ophiolite in Xiwan formed at 880 Ma. Thus we infer that the ocean between the Cathaysia Block and the Yangtze Block closed before 880 Ma, and the South China continent was assembled (Deng et al., 2012; Wang, 2000).

Stratified rocks exposed in South China mainly include two types: a basement of epimetamorphic rocks of the Sibao Group, and strata of the Shangxi Group, Shuangxiwu Group, Shuangqiaoshan Group, Lengjiaxi Group, Kunyang Group, and Huili Group. This younger cover is composed of Mid Neoproterozoic rocks formed in continental rifts and glacial events of the Late Neoproterozoic. Previous studies of magmatic rocks in South China have shown that voluminous granitic magmas were generated between 860 and 840 Ma and 830 to 750 Ma. Different views have been published of the genesis and tectonic setting of these acidic and minor basic magmatic rocks proposing that magmatism may have occurred in magmatic arcs, during orogen collapse, or intraplate continental collisions (Du et al., 2013; Li X H et al., 2012; Shen et al., 2000).

The stratified rocks in this study area are Pre-Cryogenian,

Ediacaran, Triassic, Jurassic and Quaternary strata with a distinct two-tier basement and cover structure. The basement of the folded Mesoproterozoic Kunyang Group is widely exposed, while its cover comprises a Cryogenian to Ediacaran continental molasses-continental glacial-marine clastic-argillaceous-carbonate sequence, Late Triassic continental margin offshore river-lacustrine clastic-argillaceous coal-bearing formations, and Early Jurassic argillaceous-clastic-carbonate formation in lacustrine red basins deposited under the arid climatic conditions. Magmatic activity in this area was primarily intrusive, but became eruptive later. Ninety-eight percent of the rocks are acidic rocks, and basic rocks just 2%. Intrusion of acidic magmas is characterized by multiple periods of magmatism (Ma, 1991; Xue et al., 1986).

Study of contact relationships between different rock types, hand specimens and petrography combined with unit and superunit mapping permits the Eshan granite to be divided into three intrusive parts, namely the Pojiao Unit (γ^1), the Lüzicun Unit (γ^2) and the Mokela Unit (γ^3) in descending order of age. The major rock type in the Pojiao Unit is porphyritic biotite monzogranite (samples 1–8); in the Lüzicun Unit, porphyritic biotite two-mica granite (samples 9–31); and in the Mokela Unit, biotite alkali-feldspar (tourmaline) granite (samples 32–38) (Fig. 1).

In the Pojiao Unit, porphyritic biotite monzogranite is the main rock-type of the Eshan granite. It has typical granitoid features, such as hypidiomorphic granitic texture, massive structure and mineral composition, quartz (20%–30%), acid plagioclase (30%–40%), potassium feldspar (25%–35%), biotite (10%–12%), and accessory apatite. The Lüzicun Unit (samples 9–31) occurs as scattered stocks. Its major rock type is porphyritic biotite granite containing potassium feldspar, acid plagioclase, biotite, quartz and a small amount of muscovite and hornblende. The rocks of the Lüzicun Unit are significantly finer grained than those of the Pojiao Unit. The Mokela Unit (samples 32–38) has a scattered distribution as bosses, and its major rock type is biotite alkali-feldspar granite with fine to medium grained texture, and mineral composition of predominant potassium feldspar, with plagioclase, biotite, quartz and a small amount of tourmaline.

The contact relationships of each unit and the characteristic petrography of Eshan granitoid rocks in Eshan are shown in Fig. 2. Obvious intrusive contacts are observed; the Pojiao Unit was discordantly intruded into the surrounding Kunyang Group country rocks, and is disconformably overlain by Nanhua rocks and Triassic rocks. The volume of the Lüzicun Unit is less than that of the Pojiao Unit and pulsating intrusive contacts can be observed between them. The Lüzicun Unit has locally been intruded into surrounding Pojiao-Unit rocks, and local mylonitic rocks. The Mokela Unit has a scattered and cuts the Pojiao and Lüzicun units as dykes.

2 ANALYTICAL METHODS

Rock samples from different rock types and rock masses were collected and 12 samples of different rock types were selected for analysis of major and trace elements. Sample locations shown in Fig. 1.

The samples were pulverized to below 200 mesh size, and

sent to Team 209 of Yunnan Nuclear Industry Corporation for analysis. Testing was completed at the State Key Laboratory of Continental Dynamics, Northwest University, Xi'an. Major elements were analyzed with an RIX 2100X refracted X-ray fluorescence (RXF) spectrometer auto-sampler system. Monitoring reference samples used were BCR-2 and GBW07105, and analytical error was <5%. An Agilent 7500a ICP-MS was used for

trace element analysis with BHVO-2 and AGV-2 as standard references. Accuracy of trace element test data might be up to 10%.

Samples for U-Pb analysis were processed by conventional magnetic and density techniques to concentrate non-magnetic heavy fractions. A representative selection of zircons was extracted from each concentrate by hand-picking under a binocular microscope and cast in an epoxy mount together with a

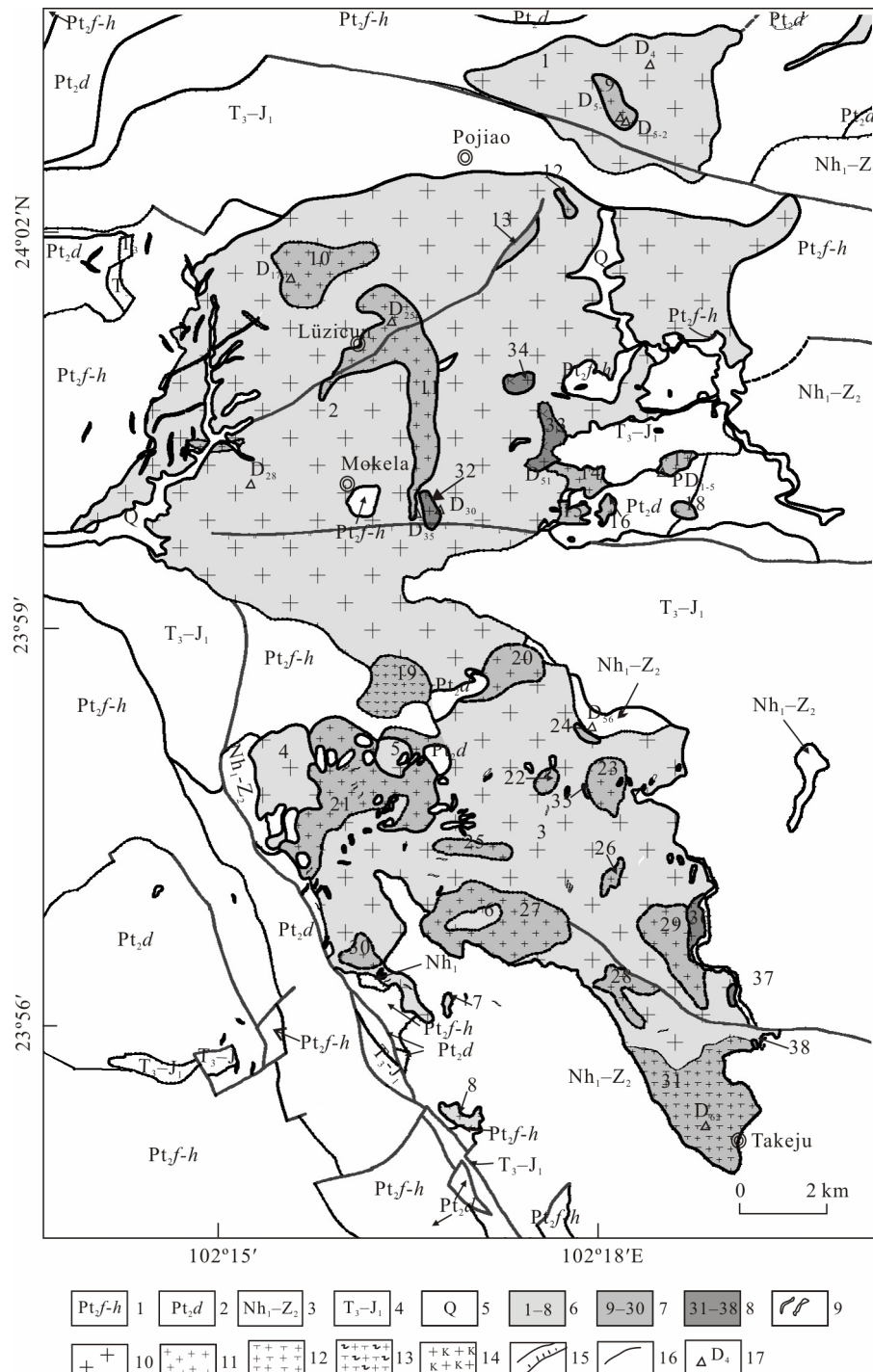


Figure 1. Geological map of the Eshan granite. 1. Proterozoic, Huangcaoling Formation-Heishantou Formation-Fuliangpeng Formation, Kunyang Group; 2. Proterozoic, Dalongkou Formation, Kunyang Group; 3. Nanhua System, Cryogenian to Ediacaran; 4. Jurassic-Triassic; 5. Quaternary; 6. Pojiao Unit, numbers indicate sample locations; 7. Lüzicun Unit and samples; 8. Mokela Unit and samples; 9. dyke; 10. porphyritic biotite monzogranite; 11. porphyritic biotite granite; 12. two mica granite; 13. tourmaline granite; 14. biotite alkali feldspar granite; 15. geological boundary and plane of unconformity; 16. fault; 17. sample locations and numbers.

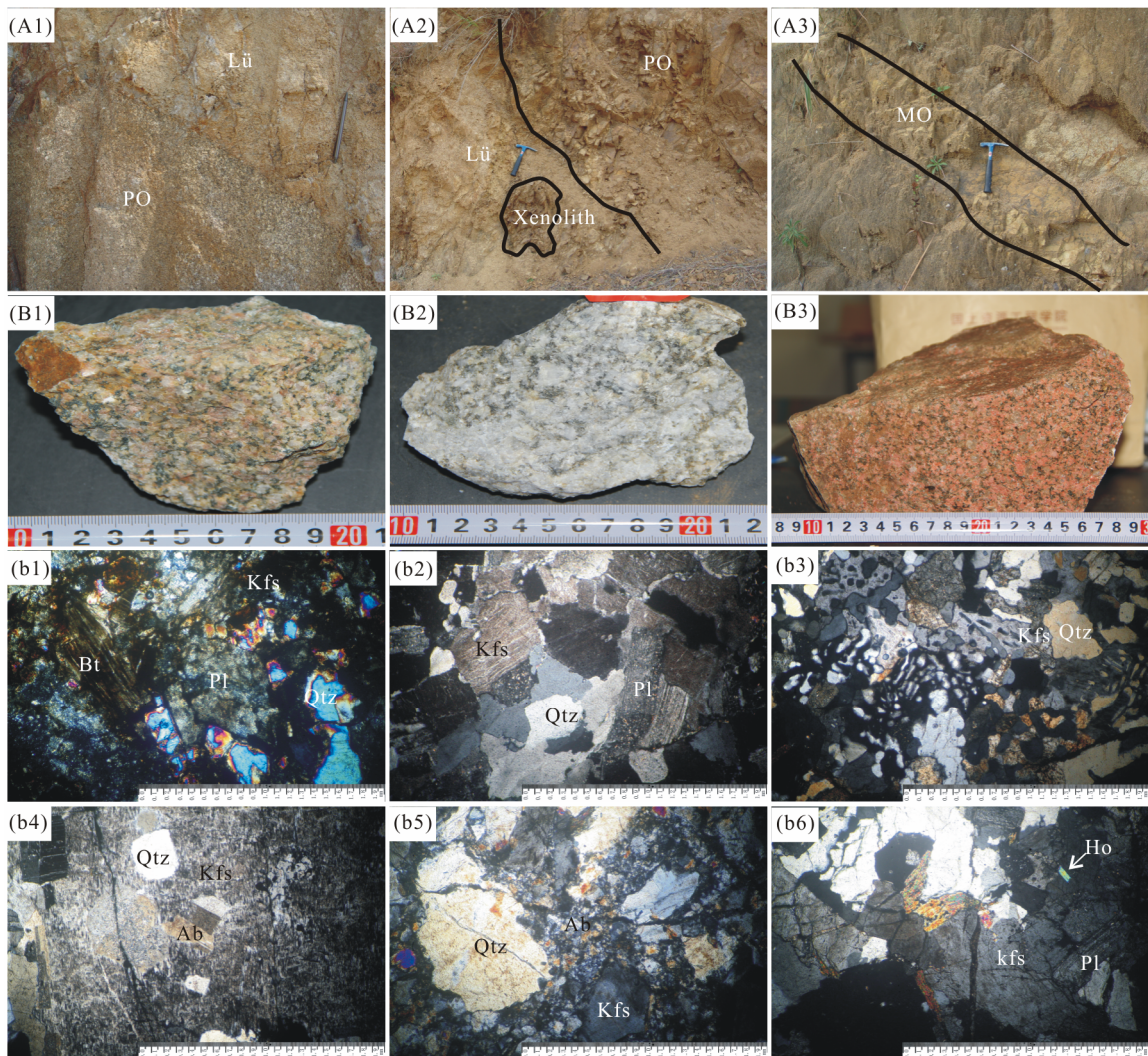


Figure 2. Photographs showing the contact relationships of each unit and characteristic petrography of Eshan granitoid rocks. PO. Pojiao Unit, Lü. Lüzicun Unit, MO. Mokela Unit. (A1) Lü intruding PO; (A2) xenolith of PO in Lü; (A3) the dyke of Mokela Unit. (B1) Porphyritic biotite monzogranite; (B2) porphyritic biotite granite; (B3) biotite alkali feldspar granite. (b1) Photomicrograph of (B1), crossed polars; (b2) photomicrograph of (B2), crossed polars, bended plagioclase; (b3) photomicrograph of (B3), graphic texture of quartz and K-feldspar phenocrysts; (b4) quartz and albite contained in K-feldspar; (b5) sucrosic albite filling between quartz and K-feldspar; (b6) hornblende in biotite granite of Lü. Kfs. K-feldspar; Pl. plagioclase; Bt. biotite; Qtz. quartz; Ab. albite; Ho. hornblende.

zircon U-Pb standard, which was then polished to section the crystals for analysis. The zircons were examined with transmitted and reflected light micrographs and cathodoluminescence images. Measurements of U, Th, and Pb were conducted using the zircon LA-ICP-MS U-Pb at the State Key Laboratory of Continental Dynamics, Northwest University, Xi'an.

3 RESULTS

3.1 Major and Trace Elements

Analyses of three Pojiao Unit samples (D28, D4, D5-2), five Lüzicun Unit samples (D17, D5-1, D25, D62, PD1-5) and four Mokela Unit samples (D35, D30, D51, D56) are shown in Table 1. Geochemical variation diagrams for each unit are shown in Figs. 3, 4, 5.

Three of the Pojiao Unit samples exhibit a limited compositional range of SiO_2 67.07 wt.%–69.12 wt.%, with corresponding K_2O contents 3.82 wt.%–4.51 wt.%, that plot in the high-K calc-alkaline field of the $\text{K}_2\text{O}-\text{SiO}_2$ diagram (Fig.

3a). All the samples are peraluminous with alumina saturation index (A/CNK) ratios of 1.12 to 1.27 (Fig. 3b). Samples of the Pojiao Unit have relatively high abundances of rare earth elements (REE) ($\Sigma\text{REE}=162 \text{ ppm}–225 \text{ ppm}$) with strong LREE enrichment and HREE depletion ($[\text{La/Yb}]_N=14.22–22.83$) (Fig. 4a). Chondrite-normalized REE patterns are characterized by high LREE ($[\text{La/Sm}]_N=5.12–5.41$), relatively flat HREE ($[\text{Gd/Yb}]_N=1.8–2.78$) and a weak negative Eu anomaly ($\delta\text{Eu}=0.64–0.83$) (Fig. 5a). Primitive mantle normalized trace element diagram shows characteristic obvious negative anomalies in Ba, P, Ti and positive anomalies in Rb, Th, U (Fig. 4a).

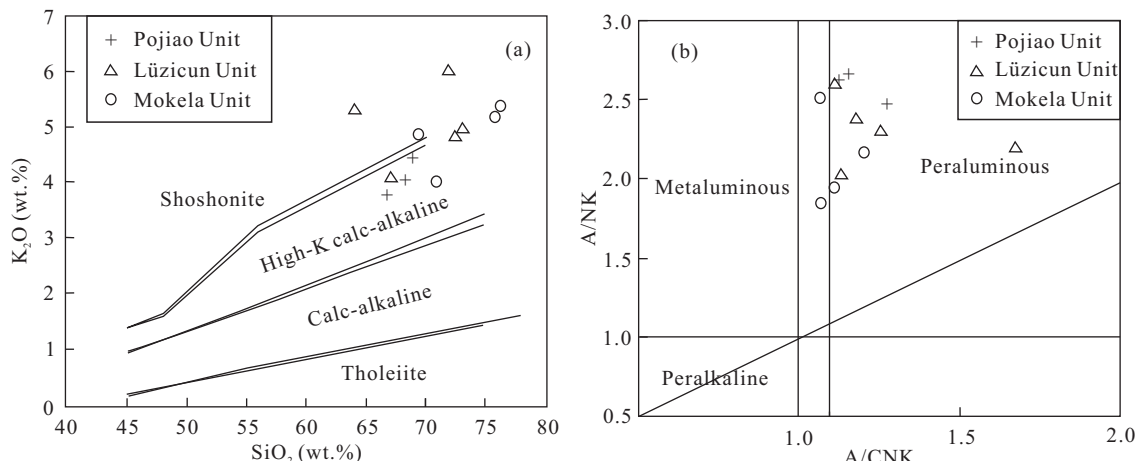
Five samples from the Lüzicun Unit have a wide compositional range of SiO_2 content 64.25 wt.%–73.4 wt.% and K_2O contents 4.06 wt.%–6.04 wt.%, and plot in the high-K calc-alkaline and shoshonite field of the $\text{K}_2\text{O}-\text{SiO}_2$ diagram (Fig. 3a). All the samples are strongly peraluminous with alumina saturation index (A/CNK) ratios of 1.13 to 1.68 (Fig. 3b). The shoshonite sample (D17) has high abundances of rare earth

Table 1 Chemical compositions of Neoproterozoic granitoids from Eshan

Unit	Pojiao Unit				Lüzicun Unit				Mokela Unit			
	D28	D4	D5-2	D17	D5-1	D25	D62	PD1-5	D35	D30	D51	D56
Major elements (wt.%)												
SiO ₂	69.12	68.69	67.07	64.25	67.32	73.4	72.7	71.92	69.44	76.29	75.88	71.14
TiO ₂	0.45	0.46	0.41	0.58	0.41	0.15	0.19	0.1	0.43	0.06	0.08	0.25
Al ₂ O ₃	14.66	15.04	14.57	16.06	15.03	14.14	14.33	12.46	14.18	13.07	12.8	14.13
TFe ₂ O ₃	4.05	4.66	5.02	5.15	4.39	2.12	2.68	5.26	4.56	1.16	1.76	3.59
MnO	0.07	0.07	0.07	0.04	0.07	0.02	0.05	0.26	0.07	0.01	0.02	0.06
MgO	1.29	1.3	1.37	1.58	1.28	0.35	0.56	0.99	1.25	0.08	0.18	0.67
CaO	1.04	1.93	1.78	1.44	1.84	0.3	0.69	0.25	0.34	0.22	0.34	1.92
Na ₂ O	2.9	3.11	3.4	3.23	3.39	3.91	2.98	0.26	3.58	3.62	3.07	3.31
K ₂ O	4.51	4.09	3.82	5.26	4.06	5.04	4.82	6.04	4.81	5.4	5.21	3.98
P ₂ O ₅	0.14	0.15	0.14	0.2	0.14	0.11	0.13	0.13	0.13	0.01	0.02	0.1
Total	99.72	100.45	99.67	99.97	99.89	100.01	100.03	99.61	99.92	100.28	99.83	99.74
K ₂ O+Na ₂ O	7.41	7.2	7.22	8.49	7.45	8.95	7.8	6.3	8.39	9.02	8.28	7.29
A/CNK	1.27	1.15	1.12	1.18	1.13	1.14	1.26	1.68	1.21	1.07	1.13	1.07
A/NK	2.49	2.67	2.62	2.37	2.61	2.02	2.30	2.18	2.16	1.83	1.93	2.50
Trace elements (ppm)												
Li	16.3	32.7	38.4	10.9	50.7	2.54	77.8	45	22.2	3.64	12.8	60.7
Be	2.6	3.66	3.6	2.67	3.57	2.02	4.7	2.81	2.68	2.49	3.19	5.69
Sc	7.82	8.62	7.21	10.1	6.93	2.74	4.23	3.12	6.78	2.41	3.2	5.63
V	57.1	57.9	53.5	77	49.4	11.2	16	6.14	43.4	4.51	4.87	29.3
Cr	19.7	21	22.7	25.5	18.7	13	13.5	11.2	15.9	9.6	6.97	11.1
Co	8.89	9.1	9.52	7.95	9.93	6.51	4.8	3.06	7.51	2.47	2.59	6.27
Ni	8.51	8.22	10.8	9.9	7.68	4.78	4.29	2.88	7.01	1.61	3.58	5.4
Cu	8.74	10.1	10.6	8.47	13.7	17.2	11.7	9.76	9.67	7.68	4.99	6.16
Zn	52.2	221	68.6	42.4	471	189	50.6	2342	42.8	24.2	10.9	38.9
Ga	17.2	18.7	17.9	19.8	17.7	15.4	17.5	13.4	14.9	15	16.2	16.9
Ge	1.35	1.67	1.51	1.65	1.54	1.36	1.84	2.64	1.04	1.77	1.91	1.82
Rb	156	176	151	137	172	176	274	286	173	246	320	212
Sr	435	399	401	339	452	178	142	72.6	259	65.1	61.3	219
Y	17.8	25.5	20.4	24.8	21.5	9.85	28.5	10.5	20.8	23.8	34.1	22.5
Zr	173	172	158	243	165	104	114	60.3	140	58.6	45.7	126
Nb	11.1	13.7	12.1	13	11.9	13	12.9	7.11	10.8	18.3	19	12.6
Cs	3.55	8.38	4.47	1.66	6.87	1.42	16	16.9	5.26	4.07	7.05	12.5
Ba	1 064	978	961	2 272	839	1 281	531	1 096	780	104	117	588
La	42.3	53.1	37.8	116	43.5	18.4	36.4	6.63	46.6	12.1	21	32.9
Ce	79.7	100	71.1	217	81.3	39.9	57.2	16.1	83.5	22.5	49	61.6
Pr	8.79	10.9	7.75	23.1	8.92	4.43	7.89	1.63	9.47	3.08	6.2	6.65
Nd	30.3	36.9	26.5	75	30.4	15.4	27.3	5.55	31.4	11.1	22.2	22.3
Sm	5.25	6.33	4.77	10.7	5.35	2.95	5.64	1.28	5.25	2.77	5.4	4.13
Eu	1.35	1.24	1.06	1.68	1.11	0.78	0.93	0.55	1.13	0.33	0.35	0.79
Gd	4.46	5.32	4.17	8.08	4.57	2.31	5.11	1.34	4.41	2.61	4.76	3.68
Tb	0.63	0.77	0.62	0.95	0.67	0.33	0.87	0.27	0.62	0.53	0.86	0.6
Dy	3.34	4.31	3.51	4.72	3.74	1.76	4.88	1.75	3.46	3.62	5.19	3.54
Ho	0.61	0.83	0.68	0.84	0.71	0.33	0.92	0.35	0.66	0.8	1.07	0.72
Er	1.63	2.35	1.93	2.29	2.01	0.97	2.45	1.04	1.89	2.53	3.11	2.1

Table 1 Continued

Unit	Pojiao Unit			Lüzcun Unit				Mokela Unit				
	D28	D4	D5-2	D17	D5-1	D25	D62	PD1-5	D35	D30	D51	D56
Trace elements (ppm)												
Tm	0.21	0.35	0.29	0.32	0.3	0.15	0.37	0.17	0.28	0.43	0.5	0.34
Yb	1.33	2.28	1.91	1.99	1.97	1.03	2.34	1.12	1.86	2.96	3.17	2.24
Lu	0.2	0.34	0.29	0.3	0.29	0.16	0.33	0.16	0.28	0.44	0.45	0.32
Hf	4.4	4.41	4.03	6.03	4.17	3.18	3.32	1.75	3.58	2.79	2.05	3.55
Ta	0.81	1.37	1.27	0.98	1.29	1.53	1.94	1.01	1.15	2.71	2.6	2
Pb	38.7	243	156	372	147	427	55.3	92.8	19.8	35.4	37.2	47.4
Th	19.4	18.7	13.5	31.8	17.6	19.8	16	4.15	15	23.4	27.8	17.2
Rb/Sr	0.36	0.44	0.38	0.4	0.38	0.99	1.93	3.94	0.67	3.78	5.22	0.97
Rb/Ba	0.15	0.18	0.16	0.06	0.21	0.14	0.52	0.26	0.22	2.37	2.74	0.36
Nb/Ta	13.7	10	9.5	13.3	9.2	8.5	6.6	7	9.4	6.8	7.3	6.3
Zr/Hf	39	39	39	40	40	33	34	34	39	21	22	35
Σ REE	180	225	162	463	185	89	142	152	191	66	123	114
LREE/HREE	13.51	12.62	11.14	22.76	11.97	11.63	9.48	7.83	13.18	3.72	5.45	5.14
(La/Sm) _N	5.2	5.41	5.12	7	5.25	4.03	5.14	4.16	5.73	2.82	2.51	2.51
(Gd/Yb) _N	2.78	1.93	1.81	3.36	1.92	1.85	1.36	1.81	1.96	0.73	1.25	1.18
(La/Yb) _N	22.83	16.74	14.22	41.85	15.88	12.79	10.53	11.15	17.94	2.94	4.76	4.45
δ Eu	0.83	0.64	0.71	0.53	0.67	0.89	0.6	0.52	0.7	0.36	0.21	0.21

**Figure 3.** (a) K_2O - SiO_2 diagram; and (b) A/NK vs. A/CNK diagram of Eshan granites.

elements (REE) (Σ REE=463 ppm) with strong LREE enrichment and HREE depletion ($La_N/Yb_N=41.85$), and a relatively weak Eu anomaly (δ Eu=0.53), and have trace element with relatively weak positive anomalies in Ba, while the other four samples have medium abundances of rare earth elements (REE) (Σ REE=89 ppm–185 ppm) and show significant LREE enrichment ($La/Yb_N=10.53$ –12.79) with a relatively weak Eu anomaly (δ Eu=0.52–0.89) (Fig. 4b). The primitive mantle normalized trace element diagram exhibits distinct negative anomalies in Ba, Sr, and HFSEs (P, Ti, Nb, Ta) and positive anomalies in Rb, Th, U (Fig. 5b).

Four of the Mokela Unit samples exhibit a wide compositional range of SiO_2 content 69.44 wt.%–76.29 wt.%, with K_2O content 3.98 wt.%–5.4 wt.%, that plot in the transition region field of high-K calc-alkaline and shoshonite in the K_2O -

SiO_2 diagram (Fig. 3a). All the samples are weakly to strongly peraluminous with alumina saturation index (A/CNK) ratios of 1.07 to 1.21 (Fig. 3b). Samples of the Mokela Unit have low abundances of rare earth elements (REE) (Σ REE=66 ppm–191 ppm) with weak LREE enrichment and HREE depletion ($La_N/Yb_N=2.94$ –17.94). The chondrite-normalized REE patterns are characterized by slightly high LREE ($[La/Sm]_N=2.51$ –5.73), relatively flat HREE ($[Gd/Yb]_N=0.73$ –1.96) and strong negative Eu anomalies (δ Eu=0.21–0.36) except D35 (δ Eu=0.71) (Fig. 4c). The primitive-mantle normalized trace element diagram shows characteristic obvious negative anomalies in Ba, Sr, and HFSEs (P, Ti, Nb) and positive anomalies in Rb, Th, U (Fig. 5c).

3.2 LA-ICP-MS U-Pb Geochronology

Four representative samples from the three units were

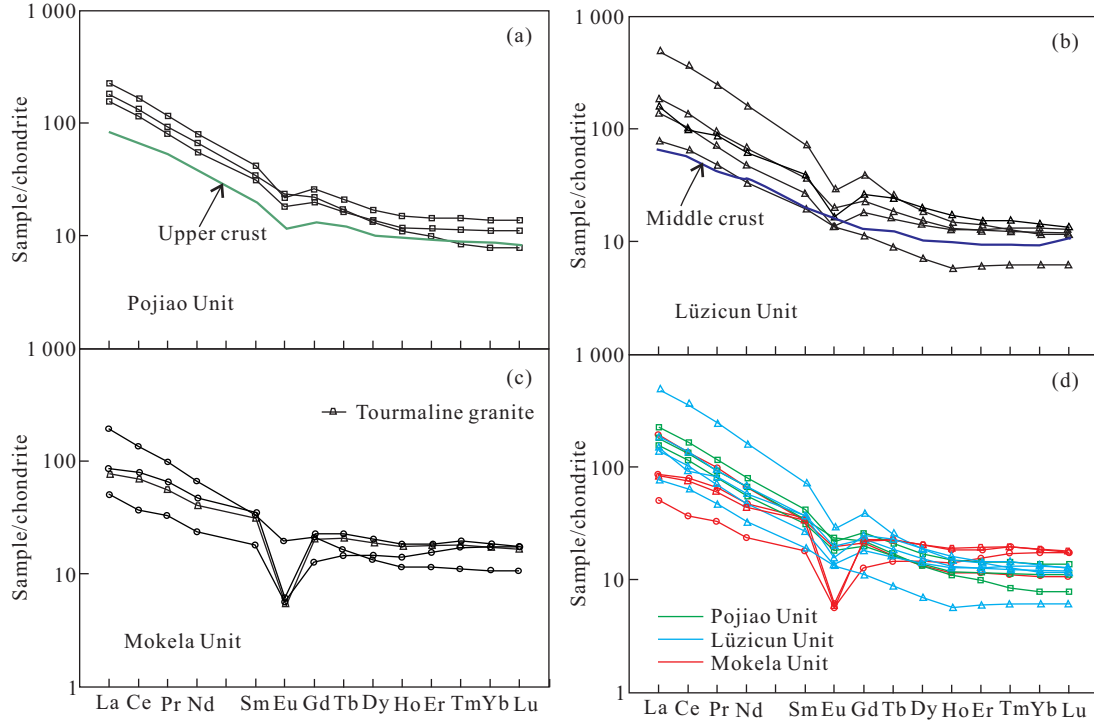


Figure 4. Chondrite-normalized REE patterns, normalization values from Sun and McDonough (1989); upper crust and middle crust values from Rudnick and Gao (2014).

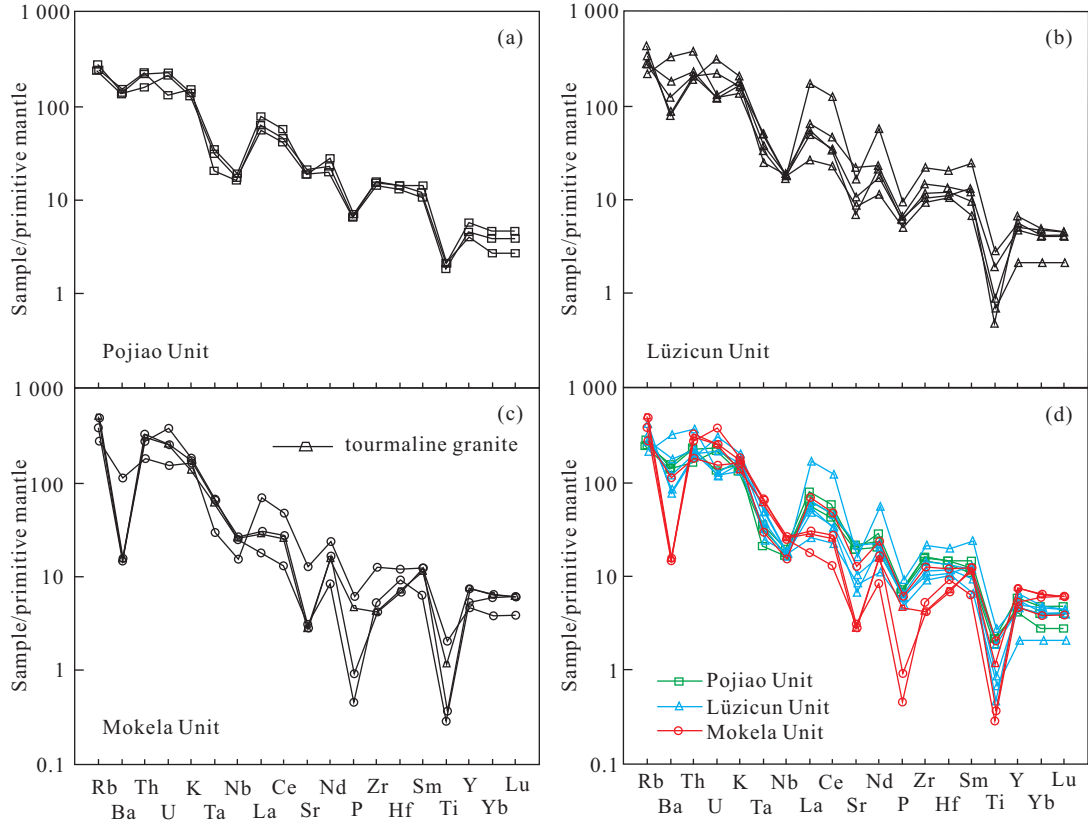


Figure 5. Primitive mantle normalized incompatible element distribution spidergrams of Eshan granites. Normalization values from Sun and McDonough (1989).

chosen, including porphyritic biotite monzogranite of the Pojiao Unit (samples D4 and D28), porphyritic biotite granite of the Lüzicun Unit (sample D17) and the biotite alkali-feldspar granite of the Mokela Unit (sample D35). The analysis results are shown in Table 3 and Fig. 6.

Zircons from D4 have inherited magmatic cores showing typical features of magmatic zircons such as clear oscillatory zoning in cathodoluminescence (CL) images (Fig. 6a), euhedral prismatic crystals with axial ratios of 2 : 1 to 4 : 1 ranging in length from 100 to 300 μm , and high Th/U ratios (0.23–0.46).

Table 2 Zircon LA-ICPMS U-Pb analysis data of the Eshan granite

Grain	Th ($\times 10^{-6}$)	U ($\times 10^{-6}$)	Th/U	Ratio				Age (Ma)					
				$^{207}\text{Pb}/^{206}\text{Pb}$	1σ	$^{206}\text{Pb}/^{235}\text{Pb}$	1σ	$^{206}\text{Pb}/^{238}\text{U}$	1σ	$^{207}\text{Pb}/^{206}\text{Pb}$	1σ	$^{206}\text{Pb}/^{238}\text{U}$	1σ
Poijiao Unit D4 (Wanhecun)													
1	151	449	0.34	0.0712	0.0025	1.4216	0.0308	0.1447	0.0020	964	71	898	13
2	150	356	0.42	0.0690	0.0022	1.3599	0.0214	0.1429	0.0018	899	65	872	9
3	154	437	0.35	0.0673	0.0022	1.3036	0.0208	0.1404	0.0018	848	66	847	9
4	151	622	0.24	0.0668	0.0021	1.2874	0.0187	0.1397	0.0018	832	64	840	8
5	119	294	0.4	0.0651	0.0021	1.2538	0.0206	0.1397	0.0018	777	67	825	9
6	135	588	0.23	0.0677	0.0022	1.1317	0.0175	0.1212	0.0015	861	66	769	8
7	110	434	0.25	0.0671	0.0023	1.0958	0.0215	0.1185	0.0016	840	70	751	10
8	217	536	0.41	0.0688	0.0022	1.1210	0.0171	0.1182	0.0015	892	64	764	8
9	397	934	0.42	0.0674	0.0022	1.0671	0.0164	0.1149	0.0014	849	65	737	8
10	351	783	0.45	0.0698	0.0023	1.0993	0.0173	0.1142	0.0014	923	65	753	8
11	206	814	0.25	0.0665	0.0022	0.9938	0.0157	0.1084	0.0014	822	66	701	8
12	329	722	0.46	0.0651	0.0021	0.9101	0.0151	0.1014	0.0013	777	67	657	8
13	313	919	0.34	0.0676	0.0022	0.9328	0.0139	0.1001	0.0012	855	65	669	7
Poijiao Unit D28 (Loli)													
1	393	1,297	0.3	0.0675	0.0022	1.5227	0.0225	0.1636	0.0020	853	65	940	9
2	111	311	0.36	0.0686	0.0021	1.3633	0.0179	0.1441	0.0017	887	63	873	8
3	91	312	0.29	0.0685	0.0021	1.3460	0.0182	0.1424	0.0017	885	63	866	8
4	147	631	0.23	0.0704	0.0022	1.3440	0.0178	0.1385	0.0017	940	63	865	8
5	283	692	0.41	0.0707	0.0022	1.2906	0.0174	0.1323	0.0016	949	63	842	8
6	320	830	0.39	0.0694	0.0022	1.1254	0.0143	0.1177	0.0014	910	63	766	7
7	156	680	0.23	0.0679	0.0021	1.0240	0.0132	0.1094	0.0013	866	63	716	7
8	166	745	0.22	0.0667	0.0021	0.9902	0.0126	0.1076	0.0013	829	63	699	6
9	23	67	0.34	0.0675	0.0021	0.8164	0.0107	0.0877	0.0011	853	63	606	6
10	398	1,272	0.31	0.0710	0.0022	0.7831	0.0100	0.0800	0.0010	958	62	587	6
11	339	1,503	0.23	0.0689	0.0022	0.7121	0.0093	0.0749	0.0009	896	63	546	5
12	245	1,080	0.23	0.0715	0.0023	0.7169	0.0101	0.0727	0.0009	972	63	549	6
Lüzicun Unit D17 (Lüzicun)													
1	251	821	0.31	0.0664	0.0021	1.3021	0.0208	0.1421	0.0018	820	66	847	9
2	204	520	0.39	0.0664	0.0023	1.2975	0.0256	0.1416	0.0018	819	70	845	11
3	213	593	0.36	0.0682	0.0023	1.3314	0.0261	0.1415	0.0018	875	70	860	11
4	277	819	0.34	0.0677	0.0022	1.3154	0.0212	0.1408	0.0018	860	66	853	9

Table 2 Continued

Grain	Th	U	Th/U ($\times 10^{-6}$)	Ratio				Age (Ma)					
				$^{207}\text{Pb}/^{206}\text{Pb}$	1σ	$^{207}\text{Pb}/^{235}\text{Pb}$	1σ	$^{206}\text{Pb}/^{238}\text{U}$	1σ	$^{207}\text{Pb}/^{206}\text{Pb}$	1σ	$^{206}\text{Pb}/^{238}\text{U}$	1σ
Luzicun Unit D17 (Luzicun)													
5	364	1 718	0.21	0.066 9	0.002 2	1.282 5	0.020 8	0.138 9	0.001 7	836	66	838	9
6	216	523	0.41	0.065 9	0.002 2	1.242 0	0.022 2	0.136 7	0.001 7	803	68	820	10
7	237	762	0.31	0.066 5	0.002 2	1.248 9	0.020 3	0.136 1	0.001 7	823	66	823	9
8	316	1 038	0.3	0.066 7	0.002 2	1.203 7	0.021 4	0.130 9	0.001 7	827	68	802	10
9	551	1 340	0.41	0.067 9	0.002 2	1.210 5	0.018 8	0.129 2	0.001 6	866	65	805	9
10	408	1 445	0.28	0.066 8	0.002 1	1.187 0	0.017 6	0.128 8	0.001 6	833	65	795	8
11	501	1 612	0.31	0.066 9	0.002 1	1.168 4	0.017 6	0.126 7	0.001 6	833	65	786	8
12	503	1 396	0.36	0.068 3	0.002 2	1.176 7	0.018 2	0.125 0	0.001 6	876	65	790	8
13	426	1 639	0.26	0.066 2	0.002 1	1.128 6	0.016 9	0.123 6	0.001 5	813	65	767	8
14	732	1 605	0.46	0.065 9	0.002 1	1.113 7	0.017 8	0.122 5	0.001 5	803	66	760	9
15	539	1 658	0.33	0.068 3	0.002 1	1.139 4	0.016 5	0.121 0	0.001 5	876	64	772	8
16	671	1 550	0.43	0.070 8	0.002 3	1.167 0	0.017 4	0.119 4	0.001 5	953	64	785	8
17	960	1 808	0.53	0.069 0	0.002 2	1.114 7	0.016 7	0.117 2	0.001 4	897	64	760	8
18	667	1 881	0.35	0.069 9	0.002 2	1.099 0	0.016 1	0.114 0	0.001 4	924	64	753	8
19	659	1 486	0.44	0.069 2	0.002 3	1.058 2	0.018 3	0.110 9	0.001 4	904	67	733	9
Mokela Unit D35 (Mokela)													
1	89	178	0.5	0.065 3	0.002 4	1.246 5	0.027 9	0.138 5	0.001 8	784	74	822	13
2	111	264	0.42	0.066 8	0.002 3	1.271 2	0.025 2	0.138 0	0.001 8	833	71	833	11
3	66	117	0.56	0.064 5	0.002 5	1.222 7	0.031 0	0.137 4	0.001 9	760	78	811	14
4	88	190	0.46	0.064 3	0.002 3	1.199 0	0.026 3	0.135 2	0.001 8	753	74	800	12
5	88	184	0.48	0.068 2	0.002 7	1.264 8	0.035 2	0.134 5	0.001 9	876	80	830	16
6	191	362	0.53	0.067 5	0.002 2	1.243 1	0.020 7	0.133 6	0.001 7	852	67	820	9
7	241	586	0.41	0.067 7	0.002 2	1.043 6	0.015 9	0.111 8	0.001 4	860	65	726	8
8	168	759	0.22	0.067 0	0.002 7	1.012 1	0.028 1	0.109 6	0.001 6	838	80	710	14
9	242	474	0.51	0.068 0	0.002 2	0.990 8	0.016 8	0.105 7	0.001 3	869	67	699	9
10	280	620	0.45	0.070 9	0.002 4	1.032 6	0.019 0	0.105 6	0.001 3	955	68	720	9
11	225	300	0.75	0.068 7	0.002 5	0.995 1	0.023 5	0.105 1	0.001 4	889	75	701	12
12	275	660	0.42	0.068 9	0.002 3	0.970 2	0.016 5	0.102 1	0.001 3	897	67	689	9
13	269	598	0.45	0.066 2	0.002 3	0.930 2	0.018 0	0.101 9	0.001 3	813	70	668	9
14	323	727	0.44	0.067 9	0.002 2	0.914 5	0.015 7	0.097 7	0.001 2	865	67	659	8
15	223	862	0.26	0.065 8	0.002 3	0.886 6	0.017 0	0.097 7	0.001 2	801	70	645	9
16	328	771	0.43	0.066 2	0.002 3	0.867 4	0.016 5	0.095 1	0.001 2	811	70	634	9

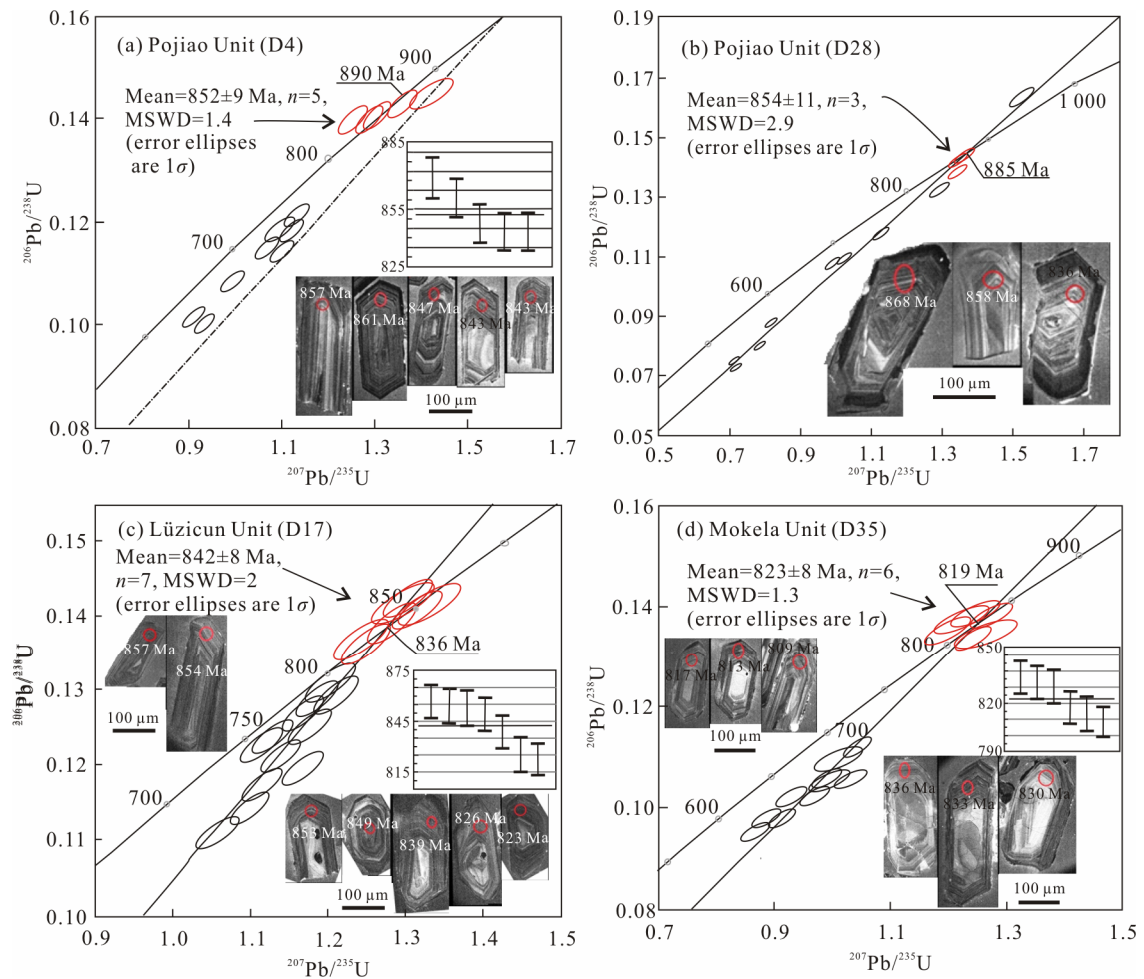


Figure 6. U-Pb concordia diagram for LA-ICP-MS analyses of the Pojiao Unit granite (D4, D28) (a), (b); the Lüzicun Unit granite (D17) (c); the Mokela Unit granite (D35) (d).

Table 3 Zircon saturation temperatures of Eshan granites

Sample	M	Zr	D _{Zr}	ln D _{Zr}	T (K)	T (°C)
Pojiao Unit						
D28	1.5	173.29	2 862.26	7.96	1 059	786
D4	1.72	171.75	2 887.98	7.97	1 042	769
D5-2	1.74	157.7	3 145.14	8.05	1 033	760
Lüzicun Unit						
D17	1.79	242.75	2 043.23	7.62	1 067	794
PD1-5	1.27	114.26	4 341.06	8.38	1 040	767
D5-1	1.74	164.51	3 015.07	8.01	1 037	764
D62	1.42	126.12	3 932.63	8.28	1 037	764
D25	1.49	104.44	4 749.30	8.47	1 017	744
Mokela Unit						
D35	1.51	139.78	3 548.37	8.17	1 040	767
D30	1.54	58.62	8 461.56	9.04	970	697
D51	1.49	45.67	10 861.67	9.29	955	682
D56	1.75	47.3	10 487.15	9.26	942	669

$$T (\text{°C}) = T(\text{K}) - 273.$$

Thirteen analyses yielded ^{207}Pb -corrected $^{206}\text{Pb}/^{238}\text{U}$ ages ranging from 871 to 615 Ma, and analytical spots yielded an upper intercept age of 885 Ma. The upper intercept magmatic group ($n=5$) yielded a weighted mean $^{206}\text{Pb}/^{238}\text{U}$ age of 852 ± 9 Ma (MSWD=1.4) (Fig. 6a). Zircons from D28 are colorless,

euhedral and prismatic, ranging in length from 100 to 300 μm with axial ratios of 2 : 1 to 3 : 1, and CL images show that zircons retain clear core-rim structures. Twelve analyses have high Th/U ratios (0.23–0.46) like those of zircons from D4, and yielded ^{207}Pb -corrected $^{206}\text{Pb}/^{238}\text{U}$ ages ranging from 977 to 452 Ma. The analytical spots yielded upper intercept ages of 890 Ma, the upper intercept magmatic group ($n=3$) yielded a weighted mean $^{206}\text{Pb}/^{238}\text{U}$ age of 854 ± 11 Ma (MSWD=2.9) (Fig. 6b). The weighted mean age of the upper intercept group indicates clearly that the Pojiao Unit has an Early Neoproterozoic crystallization age.

Zircons from D17 have inherited magmatic cores which show typical features of magmatic zircons such as clear oscillatory zoning in CL images (Fig. 6c), euhedral and prismatic crystals ranging in length from 100 to 250 μm with axial ratios of 1 : 1 to 3 : 1, and high Th/U ratios (0.21–0.53). Nineteen analyses yielded ^{207}Pb -corrected $^{206}\text{Pb}/^{238}\text{U}$ ages ranging from 860 to 733 Ma, and the analytical spots yield upper intercept ages of 836 Ma, the upper intercept magmatic group ($n=7$) yielded a weighted-mean $^{206}\text{Pb}/^{238}\text{U}$ age of 842 ± 8 Ma (MSWD=2) (Fig. 6c). The weighted mean age of the upper intercept group indicates that the Lüzicun Unit has a Middle Neoproterozoic crystallization age.

Zircons from D35 have inherited magmatic cores which show typical features of magmatic zircons such as clear oscilla-

tory zoning in CL images (Fig. 6d), euhedral and prismatic crystals ranging in length from 100 to 250 μm with axial ratios of 1 : 1 to 3 : 1, and high Th/U ratios (0.22–0.75). Sixteen analyses yielded ^{207}Pb -corrected $^{206}\text{Pb}/^{238}\text{U}$ ages ranging from 836 to 586 Ma, and the analytical spots yielded upper intercept ages of 819 Ma. The upper intercept magmatic group ($n=6$) yields a weighted-mean $^{206}\text{Pb}/^{238}\text{U}$ age of 823 ± 8 Ma (MSWD=1.3) (Fig. 6c). These data indicate that the Mokela Unit has Late Neoproterozoic crystallization ages, consistent with a reported intrusion age of ca. 819 ± 8 Ma (Li X H et al., 2003).

3.3 Crystallization Temperatures

Granite crystallization temperatures can be obtained by calculating saturation temperatures of zircon because zircon has high chemical and physical stability. It has been widely applied in U-Pb isotopic dating and geochemical tracing because it retains its composition during post-crystallization thermal events. Zircon is an accessory mineral that crystallized relatively early from granitic magma, and is frequently enclosed by younger mafic and felsic minerals. The distribution coefficients of zircon are extremely sensitive to temperature and not significantly influenced by other factors. Thus, zircon saturation temperatures approximately represent near liquidus temperatures of granitic rocks. Research on calculation of zircon saturation temperature has established an estimation model (Boehnke et al., 2013; Watson and Harrison, 1983) that we have used to model the relationship between Zr distribution and temperature by the following equation

$$\ln D_{\text{Zr}} = 12900/T(\text{K}) - 0.85 \times (M-1) - 3.80$$

where $\ln D_{\text{Zr}}$ is the distribution coefficient determined by obtaining the ratio of the zirconium abundance [Zr] of zircon (i.e., $[\text{Zr}]=496\,000$ ppm) and melt in ppm. The cited authors found that $M=(\text{Na}+\text{K}+2\text{Ca})/(\text{Al}\times\text{Si})$ is a good compositional proxy for the mechanism of zircon solution when M is calculated by obtaining the molar amounts of each component, renormalizing, and then obtaining the ratio $\ln D_{\text{Zr}}$. T (K) is absolute temperature.

Table 3 gives the zircon saturation temperatures that the calculations yielded. Three samples from the Pojiao Unit have zircon saturation temperatures values clustering at 760–785 °C, five samples from the Lüzicun Unit have relatively wide values clustering at 744–794 °C, and four samples from the Mokela Unit have values clustering at 669–767 °C.

4 DISCUSSION

The three units granite samples have similar REE and trace element compositions suggesting a possible link between them. But some different elemental ratios indicate that they are not simple products of crystallization differentiation of a homologous magma.

4.1 Petrogenesis of the Pojiao Unit—Partial Melts from Exhumed Upper Crust

As illustrated above, the Pojiao Unit granites show an S-type signature in terms of both mineral assemblage and peraluminous composition. The lack of intermediate or mafic equivalents and the chemical homogeneity suggest that the Pojiao Unit undergone little magma differentiation. The Zr/Hf

ratio is 39.0–39.3, a little higher than the 36.7 Zr/Hf ratio of upper crust (Rudnick and Gao, 2014), the Nb/Ta ratio is 9.5–13.7 near the upper crust value of 13.4 (Rudnick and Gao, 2014), and comparison of rare-earth compositions with upper crust indicate the granite magmas may have been derived by partial melting of upper crust. Low Rb/Ba (0.15–0.18) and Rb/Sr (0.36–0.44) of the Pojiao Unit granite are indicative of a clay-poor source, such greywacke partial melting (Fig. 7). Additionally, the whole-rock ratios of Sr, Nd and zircon Hf isotope signatures of porphyritic biotite monzogranite and K-rich granite from Eshan ($^{87}\text{Sr}/^{86}\text{Sr}=0.707\,2\text{--}0.715\,1$, ε_{Nd} of -6.52 to -8.43, ε_{Hf} of -2.6±0.8) (Zheng et al., 2007; Li et al., 2003) also imply that melts were derived from partial melting of ancient continental crust.

During P - T - t evolution through this partial melting process, Pojiao Unit biotite monzogranite appears to follow a decompression path with a slight temperature increase of 760 to 786 °C (Table 3, Fig. 8). Both mineral assemblages and structural relations (Fig. 2b1) show an absence of decomposition of biotite and the inverse reaction. Decompression triggered biotite dehydrated the partial melts from greywacke at temperatures 740–820 °C from 0.7 to 0.4 GPa (Wei and Zhu, 2016), and produced about 30%–40% melts (Stevens et al., 1997). So, partial melting at peak metamorphism temperature of 800 °C, and 0.5–0.6 GPa probably formed the main body of the Eshan granite.

Production of the Eshan granite has been constrained to about 880 Ma, about 30 Ma after the eruption of 920–880 Ma arc volcanics and ophiolite obduction in the eastern part of the Sibao Orogen in South China, when the Yangtze Craton was suturing to Cathaysia (Ling et al., 2003). Transpressional movement between Greater India and Western Australia may explain why all major known continental blocks had aggregated to form the Rodinia supercontinent by ca. 900 Ma (Li Z X et al., 2008). For the Pojiao Unit granite, the two weighted mean ages of upper intercept 852 ± 9 and 854 ± 11 Ma represent the timing of magma crystallization and there is an inherited Proterozoic zircon core with an age of 977 Ma, resembling tuff zircon ages of the Kunyang Group in Central Yunnan. This is evidence for a Grenvillian orogeny in Southern China (c.f., Zhang et al., 2007).

Partial melting textures developed during retrograde evolution during exhumation of upper continental crust buried to mid-crust pressure conditions (0.8 GPa) in collisional orogens have been attributed to limited partial melting at peak temperature conditions that induced weakening of the continental crust, decoupling from the lithospheric root, and initiation of exhumation (Labrousse et al., 2011). The ages of the Pojiao Unit are identical within error to the age of exhumation (Song et al., 2015). We interpret the Pojiao Unit granite as having crystallized from syn-exhumation magma that is most likely the product of melting of upper crust (Fig. 9).

4.2 Lüzicun Unit—Another Batch of Exhumed Crustal Melts but with Crustal Contamination

The Lüzicun Unit granite is slightly different from the upper crustal partial melts represented by the Pojiao Unit granite. The distinct features of biotite (two mica) granite include: (a) absence of xenoliths of Pojiao Unit granite that might indicate that crustal contamination was involved in the genesis of these

rocks. (b) The presence of albite plagioclase (observed between crossed polars) as inclusions in potash feldspar or filling between quartz and potash feldspar in biotite granite. Trondhjemite compositions are believed to trigger strength reduction and exhumation (Labrousse et al., 2011) while the presence of albite implies another batch of exhumed melts. (c) Some evidence for the compositional makeup of the middle crust comes from studies of amphibolite-facies xenoliths derived from mid-crustal depths (Weber et al., 2002). Hornblende compositions, determined in biotite granite from the Lüxicun Unit under crossed polars were likely to be present in the middle crust. (d) Peritectic reaction between muscovite and biotite, observed in crossed polars imply a muscovite dehydration melting reaction. (e) Figure 4d compares the three units' respective REE patterns. The Lüxicun Unit has a large europium anomaly compared with a weak europium anomaly of the Pojiao Unit, except for sample D25 which has no europium anomaly, and whose REE pattern is similar middle crust. The Lüxicun Unit is dominated by granite that differentiated from homologous magma of Pojiao Unit through partial melting, crystal fractionation and mixing processes (Fig. 5d compares three units' respective trace-element patterns). Like the Pojiao Unit, the Lüxicun Unit is also characterized by depletion in niobium relative to lanthanum, which is characteristic of convergent margins (Rudnick and Gao, 2014). But it has a wide range ratio of La/Nb ratios, implying mixing processes in exhumed melts. (f) One sample of the Lüxicun Unit granite gives inhomogeneous ratios of Rb/Ba (0.06–0.52) and Rb/Sr (0.38–3.94), indicative of a composition change of protolith from greywacke to shale in a clay-poor source (Fig. 7), maybe this is the reason for the heterogeneity of REE abundance in the whole Lüxicun Unit. (h) The whole-rock isotopic ratios of Sr, Nd ($^{87}\text{Sr}/^{86}\text{Sr}=0.712\ 3$, $\varepsilon_{\text{Nd}}=7.5$) of grey granite (Liu, 2016) resemble those of the Pojiao Unit, implying these melts also were derived from partial melting of ancient continental and have an S-type signature. The genesis of S-type granite can be attributed to either pure crustal melting, or hybridization of multiple magmas, could be generated by melting of pelites, metagraywackes and metaigneous rocks, or melting of metaluminous rocks with or without subsequent fractional crystallization (Chen et al., 2014). It appears that melts of the Lüxicun Unit and the Pojiao Unit derived from consanguineous magmas.

In P - T - t evolution through the partial melting process, the biotite two-mica granite of Lüxicun Unit appears to follow a decompression path with a temperature decrease of ca. 794 to 744 °C (Table 3, Fig. 8). As explained above, the absence of a muscovite dehydration melting reaction in the Lüxicun Unit indicates decompression melting under high amphibolite facies conditions at about 750 °C, less than 0.6 GPa that produced about 10% melts (Wu et al., 2015).

Therefore, the relatively young U-Pb ages (842±8 Ma) of the Lüxicun Unit is likely to be derived from partial melting of upper crust, and a slight mid crust which was triggered strength reduction by albite compositions, and both magma are mixing with crustal contamination and assimilation-fractional crystallization. It marks the other smaller batch of exhumed crustal melts.

4.3 Mokela Unit—Crustal Contaminated Residual Melts

Correlating REE and trace-element patterns from the Mokela Unit suggests that the magma primary to the Lüxicun Unit granitic magma might have experienced varying degrees of fractionation. For this alkali feldspar granitic magma, strong Eu and Ba, Sr, P, Ti anomalies imply strong fractional crystallization of plagioclase, apatite, and ilmenite. The absence of graphic granite (Fig. 2b3) indicates late stage of thermal evolution. Peritectic reaction between muscovite and biotite, observed in crossed polars in tourmaline granite, implies a muscovite dehydration melting reaction and thus a product of two-mica granitic magma fractional crystallization. Higher Rb/Ba (0.22–2.74) and Rb/Sr (0.67–5.22) ratios in the Mokela Unit granite are indicative of an

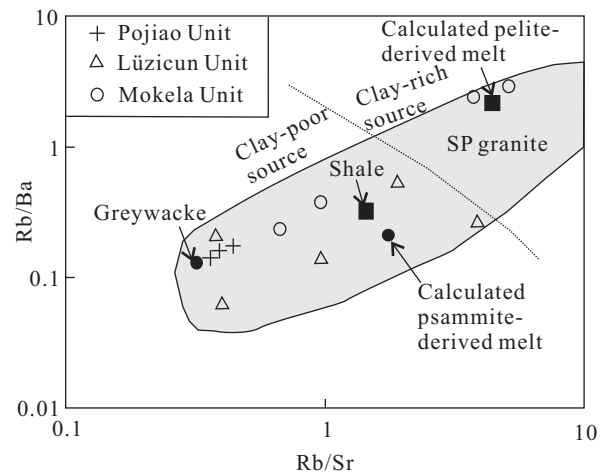


Figure 7. Rb/Sr and Rb/Ba ratios for Eshan granite (modified from Sylvester, 1998). SP. Strongly peraluminous.

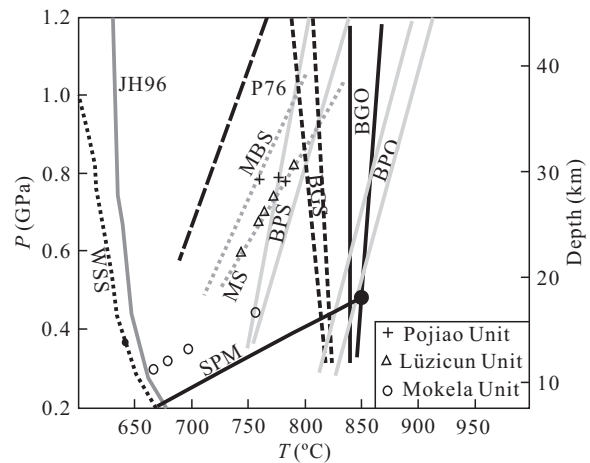


Figure 8. Pressure-temperature (P - T) diagram showing crystallization conditions of Eshan granite melts (modified from Wei and Zhu, 2016). WSS. Water-saturated solidus; JH96. experimental muscovite-albite melt is after Petö (1976); P76. experimental water-saturated solidus for leucogranite (Ab-Or-Q-H₂O) after Johannes and Holtz (1996). MBS and MS. experimental muscovite melt from two mica-schist and muscovite-schist after Patiño Douce and Harris (1998). BPS and BGS. Initial saturated solidus for biotite dehydration melts from argillaceous rock and graywacke is after Stevens et al. (1997). BPO and BGO. Stability limit line for biotite dehydration melt from argillaceous rock and graywacke is after Stevens et al. (1997). SPM. Solidus line for pelites melt after Schmidt and Poli (2014).

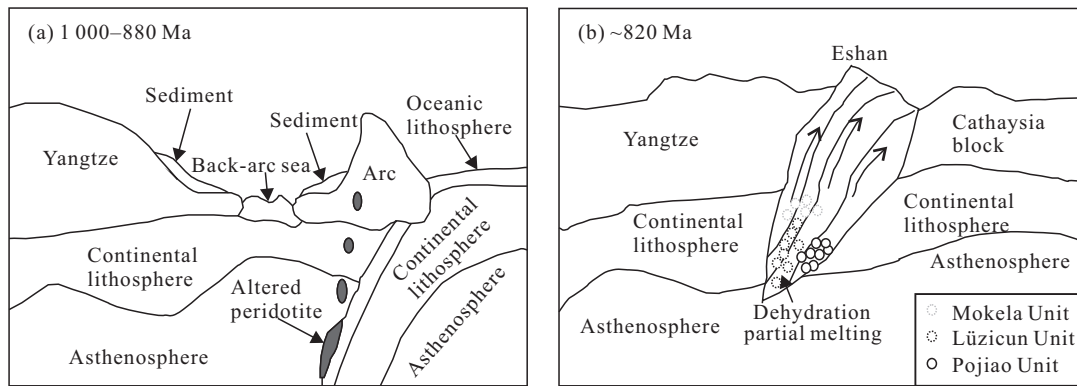


Figure 9. Tectonic evolution model for Eshan granite. (a) Continental collision of the Yangtze and Cathaysia blocks (ca. 1 000–880 Ma); (b) subduction of continental crust and multi-stage episodic magmatism in the exhumation (ca. 880–820 Ma).

inhomogeneous source of clay-poor and clay-rich derived melts that underwent subsequent mixing.

In P - T - t evolution through the fractionation crystallization process, the biotite alkali-feldspar (tourmaline) granite of the Mokela Unit appears to display a temperature decrease, ca. 767 to 669 °C, near the water-saturated solidus consistent with the solidus trend of pelite melts (Fig. 8).

The relatively younger U-Pb ages (823 ± 8 Ma) of the Mokela Unit are likely to be derived from residual assemblage and participation of argillaceous rock at the end of exhumation.

5 CONCLUSION

Post-collisional magmatism in Eshan occurred -30 Ma later than continental collision at ca. 880 Ma and shows characteristics of multi-stage episodic magmatism. Magmatism began with large-scale melting of a clay-poor source derived from subducted continental crust at ca. 854–852 Ma, followed by precipitation of albite, which is considered to have triggered strength reduction and exhumation. A later batch of exhumed melts with crustal contamination and as simulation-fractional crystallization was intruded at ca. 842 Ma, and lasted for over 20 Ma until the end of the exhumation. These differences of three units were due to consanguineous magma sources and similar processes of emplacement. The petrogenesis of the rocks in Eshan and accompanying tectonic evolution are summarized below (Fig. 9).

(a) At about 854–852 Ma, the Pojiao Unit, whose representative rock type is porphyritic biotite monzogranite, was the first emplaced granitic melt which could have resulted from slab breakoff induced exhumation of decoupled upper and lower crust, i.e., the porphyritic biotite monzogranite was most likely derived from the upper continental crust.

(b) At about 842 Ma, the Lüzicun Unit, whose representative rock types are biotite granite and two mica granite, was derived from partial melts at different continental crust levels during exhumation. The partial melts might have initiated in mid-continental crust and induced weakening of the upper-continental crust, both magmas triggering exhumation with crustal contamination.

(c) At about 823 Ma, the Mokela Unit, whose representative rock types are biotite alkali-feldspar granite and tourmaline granite with dykes, crystallized from residual melts with participation of argillaceous rock during the cooling emplaced

stage, experienced strong fractionation crystallization, and marked the final stage of exhumation.

ACKNOWLEDGMENTS

This work was supported by the Yunnan Nonferrous Geological Bureau 313 Team. Besides, we acknowledge the facility support from the State Key Laboratory of Continental Dynamics, Northwest University as well as helpful comments by reviewers and editors. Roger Mason has revised the final version. The final publication is available at Springer via <https://doi.org/10.1007/s12583-017-0747-3>.

REFERENCES CITED

- Boehnke, P., Watson, E. B., Trail, D., et al., 2013. Zircon Saturation Re-Revisited. *Chemical Geology*, 351: 324–334. doi:10.1016/j.chemgeo.2013.05.028
- Chen, Y. X., Song, S. G., Niu, Y. L., et al., 2014. Melting of Continental Crust during Subduction Initiation: A Case Study from the Chaidanuo Peraluminous Granite in the North Qilian Suture Zone. *Geochimica et Cosmochimica Acta*, 132: 311–336. doi:10.1016/j.gca.2014.02.011
- Deng, H., Kusky, T. M., Wang, L., et al., 2012. Discovery of a Sheeted Dike Complex in the Northern Yangtze Craton and its Implications for Craton Evolution. *Journal of Earth Science*, 23(5): 676–695. doi:10.1007/s12583-012-0287-9
- Du, L. L., Guo, J. H., Geng, Y. S., et al., 2013. Age and Tectonic Setting of the Yanbian Group in the Southwestern Yangtze Block: Constraints from Clastic Sedimentary Rocks. *Acta Petrologica Sinica*, 29(2): 641–672 (in Chinese with English Abstract)
- Johannes, W., Holtz, F., 1996. Petrogenesis and Experimental Petrology of Granitic Rocks. Springer, Berlin Heidelberg. 335
- Labrousse, L., Prouteau, G., Ganzhorn, A. C., 2011. Continental Exhumation Triggered by Partial Melting at Ultrahigh Pressure. *Geology*, 39(12): 1171–1174. doi:10.1130/g32316.1
- Li, X. H., Li, W. X., He, B., 2012. Building of the South China Block and Its Relevance to Assembly and Breakup of Rodinia Supercontinent: Observations, Interpretations and Tests. *Bulletin of Mineralogy, Petrology and Geochemistry*, 31(6): 543–559. doi:10.3969/j.issn.1007-2802.2012.06.002
- Li, X. H., Li, Z. X., Ge, W. C., et al., 2003. Neoproterozoic Granitoids in South China: Crustal Melting above a Mantle Plume at ca. 825 Ma?. *Precambrian Research*, 122(1–4): 45–83. doi:10.1016/S0301-9268(02)00207-3
- Li, Z. X., Bogdanova, S. V., Collins, A. S., 2008. Assembly, Configuration, and Break-Up History of Rodinia: A Synthesis Original Research Article. *Precambrian Research*, 160(1/2): 179–210.

- doi:10.1016/j.precamres.2007.04.021
- Ling, W. L., Gao, S., Zhang, B. R., et al., 2003. Neoproterozoic Tectonic Evolution of the Northwestern Yangtze Craton, South China: Implications for Amalgamation and Break-Up of the Rodinia Supercontinent. *Precambrian Research*, 122(1/2/3/4): 111–140. doi:10.1016/s0301-9268(02)00222-x
- Liu, S. B., 2016. Zircon U-Pb Geochronology, Geochemistry and Tectonic Setting of the Eshan Granite with Mo Mineralization in Yunnan Province: [Dissertation]. China University of Geosciences, Beijing (in Chinese with English Abstract)
- Ma, G. G., 1991. Isotopic Age of the Eshan Granite in Yunnan Province and Its Geological Significance. *Bull. Yichang Inst. Geol. Miner. Res.*, 16: 121–129 (in Chinese with English Abstract)
- Patiño Douce, A. E., Harris, N., 1998. Experimental Constraints on Himalayan Anatexis. *Journal of Petrology*, 39(4): 689–710. doi:10.1093/petroj/39.4.689
- Petö, P., 1976. An Experimental Investigation of Melting Relations Involving Muscovite and Paragonite in The Silica-Saturated Portion of The System $K_2O-Na_2O-Al_2O_3-SiO_2-H_2O$ To 15 kb Total Pressure. In: Progress in Experimental Petrology. NERC, London. 41–45
- Rudnick, R. L., Gao, S., 2014. Composition of the Continental Crust. In: Holland, H., Turekian, K., eds., Treatise on Geochemistry (Second Edition). Elsevier, [S.I.]. 1–64
- Schmidt, M. W., Poli, S., 2014. Devolatilization during Subduction. *Treatise Geochem.*, 4: 669–701
- Shen, W. Z., Ling, H. F., Xu, S. J., et al., 2000. Geochemical Characteristics and Genesis of Some Neoproterozoic Granitoids in the Northern Part of the Western Margin of the Yangtze Block. *Geological Review*, 46(5): 512–519 (in Chinese with English Abstract)
- Song, S. G., Wang, M. J., Wang, C., Niu, Y. L. 2015. Magmatism during Continental Collision, Subduction, Exhumation and Mountain Collapse in Collisional Orogenic Belts and Continental Net Growth: A Perspective. *Science China: Earth Sciences*, 58: 1284–1304. doi:10.1007/s11430-015-5102-x
- Stevens, G., Clemens, J. D., Droop, G. T. R., 1997. Melt Production during Granulite-Facies Anatexis: Experimental Data from “Primitive” Metasedimentary Protoliths. *Contributions to Mineralogy and Petrology*, 128(4): 352–370. doi:10.1007/s004100050314
- Sun, S. S., McDonough, W. F., 1989. Chemical and Isotopic Systematics of Oceanic Basalts: Implications for Mantle Composition and Processes. *Geological Society, London, Special Publications*, 42(1): 313–345. doi:10.1144/gsl.sp.1989.042.01.19
- Sylvester, P. J., 1998. Post-Collisional Strongly Peraluminous Granites. *Lithos*, 45(1/2/3/4): 29–44. doi:10.1016/s0024-4937(98)00024-3
- Wang, J., 2000. Neoproterozoic Rifting History of South China: Significance to Rodinia Breakup: [Dissertation]. Chengdu University of Technology, Chengdu (in Chinese with English Abstract)
- Wang, X., Erdtmann, B. D., Mao, X., 1996. 30th IGC Field Trip Guide T106/T340: Geology of the Yangtze Gorges Area. Geology Publishing House, Beijing. 73
- Watson, E. B., Harrison, T. M., 1983. Zircon Saturation Revisited: Temperature and Composition Effects in a Variety of Crustal Magma Types. *Earth and Planetary Science Letters*, 64(2): 295–304. doi:10.1016/0012-821x(83)90211-x
- Weber, M. B. I., Tarney, J., Kempton, P. D., et al., 2002. Crustal Make-Up of the Northern Andes: Evidence Based on Deep Crustal Xenolith Suites, Mercaderes, SW Colombia. *Tectonophysics*, 345(1/2/3/4): 49–82. doi:10.1016/s0040-1951(01)00206-2
- Wei, C. J., Zhu, W. P., 2016. Granulite Facies Metamorphism and Petrogenesis of Granite (I): Metamorphic Phase Equilibria for HT-UHT Metapelites/Greywackes. *Acta Petrologica Sinica*, 32(6): 1611–1624 (in Chinese with English Abstract)
- Wu, F. Y., Liu, Z. C., Liu, X. C., et al., 2015. Himalayan Leucogranite: Petrogenesis and Implications to Orogenesis and Plateau Uplift. *Acta Petrologica Sinica*, 31(1): 1–36 (in Chinese with English Abstract)
- Xue, X. H., Cai, Z. B., Xiong, J. Y., 1986. The Main Characteristics and Age Determination of E-Shan Granite in Yunnan Province. *Acta Petrologica Sinica*, 2(1): 50–58 (in Chinese with English Abstract)
- Zhang, C. H., Gao, L. Z., Wu, Z. J., 2007. Tuff Zircon SHRIMP U-Pb Age of the Kunyang Group in Central Yunnan: Evidence of Greenwill Orogenic in Southern China. *Chinese Science Bulletin*, 52(7): 818–824 (in Chinese with English Abstract)
- Zhao, Z. F., Zheng, Y. F., Dai, L. Q., 2013. Origin of Residual Zircon and the Nature of Magma Source for Postcollisional Granite in Continental Collision Zone. *Chinese Science Bulletin*, 58(23): 2285–2289. doi:10.1360/972013-636
- Zheng, Y. F., Yang, J. H., Song, S. G., et al., 2013a. Progress in the Study of Chemical Geodynamics. *Bulletin of Mineralogy, Petrology and Geochemistry*, 32(1): 1–24. doi:10.3969/j.issn.1007-2802.2013.01.001
- Zheng, Y. F., Zhang, L. F., Liu, L., 2013b. Progress in the Study of Continental Deep Subduction and Ultrahigh Pressure Metamorphism. *Bulletin of Mineralogy, Petrology and Geochemistry*, 32(2): 135–158. doi:10.3969/j.issn.1007-2802.2013.02.001
- Zheng, Y. F., Zhao, Z. F., Chen, Y. X., 2013c. Continental Subduction Channel Processes: Plate Interface Interaction during Continental Collision. *Chinese Science Bulletin*, 58(35): 4371–4377. doi:10.1007/s11434-013-6066-x
- Zheng, Y. F., Zhang, S. B., Zhao, Z. F., et al., 2007. Contrasting Zircon Hf and O Isotopes in the Two Episodes of Neoproterozoic Granitoids in South China: Implications for Growth and Reworking of Continental Crust. *Lithos*, 96(1/2): 127–150. doi:10.1016/j.lithos.2006.10.003
- Zhou, J. C., Wang, X. L., Qiu, J. S., 2005. The Characters of Magmatism in the Western Section of the Jiangnan Orogenic Belt. *Geological Journal of China Universities*, 11(4): 527–533. doi:10.3969/j.issn.1006-7493.2005.04.008 (in Chinese with English Abstract)
- Zhou, M. F., Yan, D. P., Kennedy, A. K., et al., 2002. SHRIMP U-Pb Zircon Geochronological and Geochemical Evidence for Neoproterozoic Arc-Magmatism along the Western Margin of the Yangtze Block, South China. *Earth and Planetary Science Letters*, 196(1/2): 51–67. doi:10.1016/s0012-821x(01)00595-7